Seafloor Overthrusting Causes Ductile Fault Deformation and Fault Sealing Along the Northern Hikurangi Margin

Julia K. Morgan[1], Evan A. Solomon[2], Ake Fagereng[3], Heather M. Savage[4], Maomao Wang[5], Francesca Meneghini[6], Philip M. Barnes[7], Rebecca Bell[8], Melodie French[1], Nathan Bangs[9], Hiroko Kitajima[10], Demian M. Saffer[9], and Laura M. Wallace[9,11]

(1) Rice University, Houston, TX, United States, (2) University of Washington, Seattle, WA, United States, (3) Cardiff University, School of Earth and Environmental Sciences, Cardiff, CF10, United Kingdom, (4) University of California, Santa Cruz, CA, United States, (5) Hohai University, Nanjing, China, (6) University of Pisa, Pisa, Italy, (7) National Institute of Water & Atmospheric Research, Wellington, New Zealand, (8) Imperial College London, London, SW7, United Kingdom, (9) University of Texas at Austin, Institute for Geophysics, Austin, United States, (10) Texas A & M University, College Station, TX, United States, (11) GNS Science, Lower Hutt, New Zealand

---

Abstract

IODP Site U1518, drilled during IODP Expeditions 372 and 375, penetrated a large-offset (~6 km) thrust, the Pāpaku fault, rising from a megathrust that hosts recurring slow slip events along the Hikurangi margin. Although drilling intersected the fault zone at only ~300 m below the seafloor within porous silty mudstone, it exhibits intense tectonic ductile deformation, including finely banded mudstones contorted into decimeter-scale folds; elongate mudstone clasts with grain tail complexes; stacked and truncated silt beds in distorted mudstones; and soft sediment injections. Locally, these ductile features are overprinted by brittle deformation, including normal faults, fracture arrays, and breccias. The more consolidated hanging wall is dominated by brittle structures, whereas the footwall exhibits ductile and brittle deformation that decreases in intensity with depth. The intense tectonic ductile deformation and asymmetric distribution of structures across the fault zone at Site U1518 can be explained by seafloor overthrusting. The emplacement of the hanging wall upon the footwall flat overrode high-porosity, undeformed, and previously unburied sediments, localizing shear deformation within these weak sediments. In contrast, the overconsolidated hanging wall preferentially experienced brittle deformation during folding and displacement. Interstitial pore water geochemical profiles

at Site U1518 show a repetition of near-seafloor diagenetic sequences below the fault, consistent with overthrusting of previously unburied strata. The preserved diagenetic profiles in the footwall suggest that overthrusting occurred within the last 50-100 kyr, and indicate little along- or across-fault fluid flow at the location of Site U1518. Thus the Pāpaku fault appears to define a low-permeability seal that restricts footwall consolidation, maintaining locally high pore fluid pressures and low fault strength. If similar low permeability structures occur elsewhere along the margin, they could support regionally high pore pressure conditions favorable to the occurrence of SSEs on the Hikurangi megathrust fault.

Keywords: Forearc deformation, overthrusting, ductile sediment deformation, fault processes, fluid flow

1. Introduction

Accretionary prisms preserve a record of deformation processes at convergent margins. A fundamental question in such settings is how and why strain is partitioned within and beneath the prism, and how such partitioning affects fault slip behavior and associated hazards (e.g., Park et al., 2002; Martin et al., 2010; Greve et al., 2020). Some faults exhibit significantly greater displacements than others, posing the possibility that slip on these faults correlates with higher risk of earthquakes or tsunamigenesis (e.g., Lay et al., 2005; Moore et al., 2007). Furthermore, the distribution and mode of deformation may strongly influence the distribution of pore fluid pressures and fluid flow within and across the margin (e.g., Tobin et al., 2001; Saffer and Tobin,

2011; Kastner et al., 2014; Fagereng et al., 2018), with implications for the types of fault slip behavior that may occur (Saffer and Wallace, 2015).

Drilling at the northern Hikurangi Margin during International Ocean Discovery Program Expeditions 372 and 375 (Wallace et al., 2019) provided an unprecedented opportunity to study these topics in a setting known to host both repeating slow slip events (SSEs; Wallace and Beavan, 2010; Wallace et al., 2016) and tsunami earthquakes along the shallow megathrust (Doser and Webb, 2003). In particular, coring and logging-while-drilling (LWD) at Site U1518 penetrated the ~6 km offset Pāpaku thrust fault at a depth of ~300 m below the seafloor (mbsf). The fault is characterized by a zone of ductilely deformed fine-grained hemipelagic sediments, with modest brittle overprint (Fagereng et al., 2019; Saffer et al., 2019; Cook et al., 2020). As the Pāpaku thrust soles into the megathrust near the interpreted source area of some SSEs (Wallace et al., 2016; Barker et al., 2018; Barnes et al., 2020), these observations suggest that the combination of ductile and brittle deformation within the fault zone reflects variable slip behaviors (e.g., Fagereng et al., 2019). There also may be unique conditions that favor ductile sediment deformation in this shallow fault setting, which we explore further through combined analysis of core data and interpretations of a co-located seismic reflection profile.

Here, we use core observations and porosity measurements collected on Expeditions 372 and 375 to examine the distribution of deformation across the Pāpaku fault. Based on seismic interpretations of the frontal wedge, we propose a simplified kinematic evolution, concluding that the hanging wall of the Pāpaku fault overthrust the seafloor producing a classic "ramp-on-flat" hanging wall – footwall configuration (Boyer and Elliott, 1982; Suppe, 1983). The process of consolidated hanging wall overthrusting a poorly consolidated, porous footwall can explain the intense ductile shearing observed within the fault zone, the contrasting deformation histories

of the hanging wall and footwall, and other distinctive characteristics of this system. Pore fluid geochemical profiles across the fault zone support this explanation, suggest that overthrusting occurred within the last 50-100 kyr, and that presently, the Pāpaku fault is a barrier to fluid flow.

2. Geological Setting

Expeditions 372 and 375 drilled a transect of sites across the Northern Hikurangi Margin (Figures 1) where the Hikurangi Plateau, a Cretaceous large igneous province, is subducting westward beneath the North Island of New Zealand at ~5 cm/yr (Wallace et al., 2004). Although the northern part of the margin is primarily non-accretionary (Collot et al., 2001), a ~1-2 km thick Cenozoic to Mesozoic sedimentary sequence is partially accreted in the vicinity of Site U1518 (Figure 1). Megathrust slip is accommodated primarily by shallow repeating SSEs that occur every 18–24 months in this location (Wallace and Beavan, 2010). Recent seafloor geodesy suggests slow slip may reach within ≤2 km of the trench along the Expedition 375 drilling transect (Wallace et al., 2016), although the exact structures that accommodate slip are not known. Constraining the causes and consequences of such SSEs was a primary motivation for these Expeditions.

A portion of the time-migrated, depth-converted seismic profile 05CM-04 is shown in Figure 1c, with interpretations from Barnes et al. (2020) and Davy et al. (2021). The Pāpaku fault is characterized by a steeply dipping landward fault segment that transitions into a gentler dipping (~10°) seaward segment. A prominent fault-bend fold has developed in the hanging wall of the fault. In contrast, footwall reflections are oriented approximately parallel to the seaward fault segment. Offset stratigraphic reflections, including horizon BSU4, provide a first-order

estimate of apparent displacement on the Pāpaku fault of ~6 km (Barnes et al., 2020). Site U1518 penetrated the seaward extent of the Pāpaku fault, about 0.5 km from where the fault emerges at the seafloor along a steep slope marked by truncated reflections, indicating removal of strata by landslides (Saffer et al., 2019) (Figure 1c). Two seaward thrust faults exhibit lower fault offsets and smaller hanging wall folds. Small offset faults are interpreted in the hanging wall of the Pāpaku fault near the fault kink (Figure 1c) and additional splay faults have been identified using full-waveform inversion reflection images of the 2018 NZ3D data (Davy et al. 2021).

3. Site U1518 Overview

As detailed in Saffer et al. (2019), LWD data from Hole U1518B, drilled to a depth of 600 m below seafloor (mbsf) during Expedition 372 suggest the primary fault zone lies between 315 and 348 mbsf (Cook et al, 2020). Two boreholes (U1518E and F) about 50 m to the south were cored during Expedition 375 (Figure 2a). Hole U1518E sampled the hanging wall down to ~200 mbsf, but severe drilling disturbance prevented identification of primary structures. Hole U1518F provided reasonable core recovery (43%) to a depth of 492.3 mbsf, sampling the lower hanging wall, the soft-sediment Pāpaku fault zone, and the footwall. The hanging wall (lithological Unit I) is composed of silty to clayey, normally graded turbidites and hemipelagic sediment, and intermittent tephra layers (Figure 2b). The uppermost footwall (lithological Unit II) has a similar composition but with fewer silt beds, and the deepest footwall (Unit III) exhibits dispersed contorted beds suggestive of syn-depositional soft-sediment deformation. Based on shipboard observations of recovered cores, the main strand of the Pāpaku fault was identified at 304.5-322.4 mbsf and a subsidiary fault at 351.2-361.7 mbsf (Figure 2). Biostratigraphy reveals

123 an age inversion across the main fault; the base of the hanging wall is dated at 0.67 ma, whereas
124 the top of the footwall is estimated at ~0.31 ma (Crundwell and Woodhouse, 2022). A second
125 age inversion at ~185 mbsf hints at a shallow splay fault within the hanging wall (Davy et al.,
126 2021) that was not detected in drill cores.

127 Porosities measured on discrete shipboard samples generally decrease with depth through
128 Holes U1518E and F (Figure 2c), but exhibit significant variation due to lithologic and structural
129 changes. In the shallowest hanging wall, mean porosities are ~55%, decreasing to ~41% just
130 above the main fault zone. Mean porosities step up to ~46% within the fault zone, remain at ~44-
131 45%, between the two faults, then decrease slightly within the subsidiary fault. Mean porosities
132 increase to ~50% at the base of the subsidiary fault zone, and decrease unsteadily across the
133 footwall, reaching 40-45% at the base of the hole. Thus, both the top and base of the interval
134 containing the fault zones are marked by steps up in porosity of up to 5% and 7%, respectively.
135 The trends in shipboard sample porosities are in general agreement with Neutron porosities
136 measured in the LWD data from Hole U1518B (Cook et al, 2020), but the absolute values of the
137 discrete samples are a few percent lower shallower than ~200 mbsf (Figure 2c), likely due to
138 intense drilling disturbance throughout Hole U1518E. LWD porosities are noticeably higher in
139 the shallow footwall, from 370-450 mbsf, possibly due to porosity variations between the holes
140 or overestimated LWD porosities due to enlarged borehole diameter.

141 Structural domains identified in the core coincide closely with the lithostratigraphic units
142 determined shipboard (Figures 2d and e). The hanging wall is characterized by variable bedding
143 dips, with zones of inclined bedding dipping up to ~60° and locally overturned, indicative of
144 broad folding. More consistent bedding dips of ~30° or less occur within the fault zones and
145 footwall, with dips generally decreasing with depth. Fractures and faults occur throughout the

146 core, but are most abundant and variably oriented within the hanging wall (Savage et al., 2021).
147 Locally, zones of intense brecciation occur, particularly within the two fault zones.
148
149 **4. Characteristics of the Pāpaku Fault Zone and Adjacent Domains**
150
151 The distinct physical properties and structural characteristics of the hanging wall and
152 footwall (Figure 2) point to contrasting deformation histories of these two domains, structurally
153 separated by the Pāpaku fault. Figure 3 presents a generalized interpretation of Cores 375-
154 U1518F-13R through the upper part of -15R, covering the interval identified as the main fault
155 zone and revealing downhole distributions of deformation. Representative close-up core photos
156 in Figure 4 highlight some of the key features discussed below.
157
158 *4.1. Hanging Wall*
159 The hanging wall is preserved at the top of Core 375-U1518F-13R (Figure 3) and displays
160 characteristics consistent with shallower cores from Hole U1518F (Saffer et al., 2019). This
161 domain is composed of cohesive sediment cut by abundant healed fractures and faults (blue
162 lines, Figure 3). Cross-cutting structures of different types and orientations demonstrate multiple
163 phases of brittle deformation. Minor faults exhibit mm- to cm-scale apparent offsets, typically
164 with normal displacements (Figure 4a). Several intensely brecciated zones occur with fracture
165 networks defined by mm-scale fracture spacing, often with no obvious shear displacement
166 (Figures 3 and 4a). The density of fractures within the hanging wall generally increases with
167 depth, with zones of locally higher fracture density occurring ~10-20 m above the fault zone
168 (Fagereng et al., 2019; Savage et al., 2021).

169

170 *4.2. Primary Fault Zone*

171 The main fault zone is characterized by a mixture of ductile and brittle deformation (Figure
172 3). The types of observed structures are described in detail in Fagereng et al. (2019) and only
173 briefly summarized here. The ductile deformation features fall into several categories, with
174 characteristics that distinguish them as products of intense tectonic shearing rather than syn-
175 depositional soft-sediment deformation. The predominant ductile structures are classified as
176 "flow-banding", which includes parallel layers of sediments ranging in scale from sub-mm
177 laminations up to ~5 mm thick color bands (green lines in Figure 3), dismembered sedimentary
178 layers, in particular silt beds (gray bands in Figure 3), elongate sedimentary clasts, and apparent
179 grain tail complexes. These ductile deformation features are interpreted to result largely from
180 bedding-parallel ductile shear flow accommodated by sediment disaggregation, comminution,
181 and particulate flow, and are well developed throughout the main fault zone (green lines in
182 Figure 3). Locally, brittle structures such as fractures, faults, and brecciation, disrupt layering
183 and overprint the ductile features, demonstrating multiple phases of tectonic deformation. As the
184 drilling process can also cause brittle deformation, we distinguish tectonic brittle structures as
185 those that are now sealed, or fractures and faults that span the core with offsets or slip indicators
186 that cannot be caused by drilling.

187 In this study, the top of the main fault zone is re-interpreted at 375-U1518R-13R-1, 100 cm,
188 at a sharp downhole transition from fractured hanging wall to a zone with variably oriented color
189 banding that lacks overprinting fractures (Figure 4c). This transition marks the first clear-cut
190 occurrence of flow-banding at a depth of 304.20 mbsf, 30 cm shallower than previously
191 interpreted (Saffer et al., 2019; Fagereng et al., 2019). This judgement is based on the lack of

such flow-banding above this point. The occurrence of very finely laminated flow-banded mudstone is the most distinctive characteristic of the main fault zone (green lines, Figure 3). Locally, these flow-banded zones also exhibit mm-scale asymmetric clasts with tails (e.g., Figure 4e), and may be further contorted into decimeter-scale folds (e.g., Figure 4e), indicating local non-planar shear deformation.

Tectonic brittle deformation occurs throughout the primary fault zone. Examples include small-offset normal faults that cross-cut coarse planar flow-banding (Figure 4h), as well as distorted and truncated stacks of mudstones and silt layers cross-cut by fine filled fractures near the top of the faulted interval (Figure 4g). Zones of intense sediment brecciation (red x in Figure 3), possibly caused or enhanced by drilling disturbance, locally preserve the underlying flow-banding (Figure 4d), confirming an earlier history of ductile shearing.

Several features within the main fault zone suggest fluidization of soft sediments (pink bands in Figure 3). These include divergent sediment stringers sandwiched between zones of planar flow-banding (Figure 4d), disaggregated sediment injected into adjacent cohesive sediment (Figure 4f), and local occurrences of homogenized gray material, e.g., within a flow-banded unit, now cross-cut by small-offset normal faults (Figure 4h).

Notably, the discrete silt beds (gray bands) observed within the hanging wall are generally absent throughout the fault zone, with the exception of a package of stacked and contorted muds and silts (Interval U1518R-14R-1A, 109-150 cm, Figure 4g). The few silt beds that occur within the fault zone are highly distorted, dismembered and offset along small faults.

Based on the occurrence of well-developed flow-banding, the primary fault zone is interpreted to extend to the base of Core 375-U1518R-14 (322.4 mbsf), encompassing a domain up to ~18 m thick. However, due to incomplete core recovery (Figure 2) significant material is

missing and the exact thickness of the fault zone is unknown. This compares with an interpreted fault zone thickness of ~33 m (315-~348 mbsf) interpreted in the LWD data in Hole U1518B, 50 m to the north, based on boundaries of bedding orientation domains (Cook et al., 2020).

4.3. Footwall

Below the main fault zone, at the top of Core 375-U1518F-15R, the character of the sediment changes and deformation decreases in intensity (Figure 3). Coarse flow-banding is still evident, but the domains of mm scale laminations are absent. Distinct ductile deformation features of various types persist, including convolute layering, sharp bedding truncations, and rare injection features, but they are not well developed. These features generally occur within otherwise coherent strata, indicating that they are not due to drilling disturbance. The density of fractures within this domain is reduced relative to the lower hanging wall and the primary fault zone (Figure 2 and Savage et al., 2021), although small-offset normal faults occur. Irregular zones of homogeneous gray material lacking internal fabric occur, with boundaries that truncate sedimentary horizons. In at least one example, the gray material was injected into the surrounding sediment in the plane of split core (Figure 4i). These features may reflect fluidization of soft sediments, likely remobilized during shearing along the fault. The sharply bounded, homogenized sediment in Figure 4i is also cross-cut by a planar black band and small-offset normal faults, demonstrating brittle overprinting. Thin silt beds appear again, locally dismembered (Figure 4j) or distorted into small recumbent folds (Figure 4k).

Between 351.2 and 361.7 mbsf, deformation intensity increases again, defining a subsidiary fault that cuts through the footwall with no obvious lithologic or age change (Fagereng et al., 2019). This feature may correlate with a possible subsidiary fault zone interpreted in LWD at

~369 mbsf in Hole U1518B (Cook et al., 2020). Flow-banding is less intense than in the main fault, although several mud clasts exhibit elongate asymmetric tails that suggest non-coaxial shear deformation (Figure 4l). Locally, discrete faults juxtapose convolute beds or banding of different orientations. The subsidiary fault zone boundaries are poorly defined, instead deformation intensity gradually decreases with distance. Deeper occurrences of flow-banding, contorted bedding, and fractures are rare, and may relate to additional subsidiary faults (Cook et al., 2020) or syn-depositional soft-sediment deformation (Saffer et al., 2019).

5. Origin of Ductile Fault Deformation and Kinematics of the Pāpaku Fault System

The distinct contrasts in structural styles between the hanging wall and footwall of the Pāpaku fault system, and prevalence of intense tectonically-induced ductile sediment deformation are atypical in most shallow fault zones previously drilled at subduction forearcs (e.g., Lundberg and Moore, 1986; Taira et al., 1992; Kirkpatrick et al., 2014). One exception is the frontal décollement zone along the Costa Rica margin drilled during Leg 170 (Tobin et al., 2001), where the more consolidated lower slope wedge overrode less consolidated, higher porosity trench sediments. Similar to the Pāpaku fault, the upper plate at Costa Rica is characterized by brittle fractures, faults, and deformation bands, whereas the uppermost underthrust section experienced ductile shearing (Vannucchi and Tobin, 2000). The example of the cohesive Costa Rica wedge superposed upon less consolidated trench sediments offers helpful perspectives about accretionary processes along the northern Hikurangi margin.

Structural and stratigraphic geometries exhibited in seismic profile 05CM-04 (Figure 1c) clarify the evolution of the Pāpaku fault system. Displacement along the Pāpaku fault is

261 estimated at ~6 km, much greater than the initial thickness of the incoming sedimentary section
262 (Barker et al., 2018; Barnes et al, 2020). Thus, the hanging wall ramped through the entire
263 incoming section, and overthrust the seafloor. Presently, the hanging wall ramp defines the base
264 of the hanging wall fault-bend fold, and is superimposed upon a footwall flat parallel to the
265 underlying strata (Figure 1c). This geometry defines a classic ramp-on-flat configuration of an
266 overthrust fault (Boyer and Elliott, 1982; Suppe, 1983). To first order, the hanging wall ramp
267 overrode the undeformed seafloor a distance of at least 3 km.

268 Figure 5a presents a simplified kinematic evolution of the frontal prism that broadly
269 reproduces this configuration. Progressive displacement of the landward edge of a package of
270 sediments (Stage 1) activated the Pāpaku fault, which ramped through the incoming strata (Stage
271 2), eventually emerging onto and sliding along the seafloor (Stage 3), undergoing folding above
272 the ramp-flat kink in the fault. At that point, the seafloor became the thrust fault, accommodating
273 continued displacement of the hanging wall. Continued convergence activated two more seaward
274 thrust faults, which exhibit less displacement (Stage 4). This schematic model explains the
275 evolution of the fault system to first order and highlights several interesting features. As the
276 hanging wall of the Pāpaku fault slid over the footwall flat, fault length increased progressively
277 as new seafloor was incorporated into the fault zone. Thus, both the magnitude of slip along the
278 footwall flat and age of the fault decrease in the seaward direction; they are highest at the ramp-
279 flat kink and reach zero where the fault intersected the original seafloor. Furthermore, at Site
280 U1518, the hanging wall has been displaced significantly farther than the footwall, and thus
281 experienced a longer history of tectonic deformation.

282 Site U1518 (vertical black bar in Stage 4) penetrated the shallowest reaches of this fault,
283 ~0.5 km from where it now intersects the seafloor. Truncation of shallow horizons in the seismic

284 profile (Figure 1c) suggests landslide removal of some of the hanging wall. Depending on when
285 landsliding occurred and amount of material removed, the original tip of the fault may have been
286 seaward of the current seafloor intersection by as much as ~1.5 km. Thus fault displacement at
287 Site U1518 could range from ~0.5-1.5 km.

288 The schematic kinematic evolution in Figure 5a clarifies why the hanging wall and footwall
289 at Site U1518 experienced such contrasting deformation histories, and provides insights into the
290 origin of the intense ductile deformation along the Pāpaku Fault. Two small rectangles track
291 representative positions of the hanging wall (dashed) and footwall (solid gray), until they become
292 superimposed in Stage 4. A plausible evolution of these representative domains at each
293 kinematic stage of deformation is shown in Figure 5b.

294 Prior to Stage 1 and onset of tectonic loading, the deepest hanging wall strata at Site U1518
295 were buried to a depth of more than 300 m. At Stage 1, thrust faulting initiated under tectonic
296 loading, accompanied by brittle deformation and distributed wall rock damage typical along
297 faults within cohesive lithologies (e.g., Meneghini and Moore, 2007; Savage and Brodsky,
298 2011). Stage 2 captures uplift of the hanging wall and onset of time-transgressive folding as it
299 passed through fault-bend kinks linked to the footwall ramp-to-flat transition (Suppe, 1983). This
300 folding and unfolding caused additional local fracturing (Cosgrove, 2015).

301 By Stage 3, the shallowest hanging wall had overthrust poorly consolidated seafloor
302 sediments. The superposition of the hanging wall upon these previously undeformed porous
303 strata, shifted shear deformation into the weaker footwall unit. Footwall sediments may have
304 experienced further consolidation due to burial beneath the hanging wall. Given the initially high
305 porosities and low effective stresses in the shallowest footwall sediments, ductile deformation
306 would have been favored in the footwall (Muir Wood, 1991). This contrasts with the brittle

deformation and off-fault damage commonly associated with forearc thrust faults, as now preserved in the hanging wall of the Pāpaku fault (Savage et al., 2021). Rapid loading of porous footwall sediments may have generated excess pore pressures capable of causing local sediment fluidization, injection, and fracturing, schematically shown in Stages 3-4 in Figure 5b. Although the underthrust sediments are expected to dewater over time, pore fluid dissipation depends on the loading rate and sediment permeability, neither of which is well constrained. However, steps up in porosities within and across the Pāpaku fault in shipboard and LWD data (Figures 2), and interpreted from geophysical data (Gray et al, 2019; Cook et al., 2020), suggest that the footwall is underconsolidated relative to the hanging wall, and likely still supports excess pore fluids (French and Morgan, 2020).

Emplacement and displacement of the hanging wall along the Pāpaku fault were likely associated with ongoing slope failure, as in other accretionary settings (Strasser et al., 2011; Moore et al., 2019). Removal of shallow sediments reduced the vertical stress within the hanging wall and fault, enabling brittle deformation (Muir Wood, 1991) that enhanced fracturing of the hanging wall, and overprinted earlier ductile deformation in the fault zone. Sediments sloughed off the slopes were entrained into the fault zone as the hanging wall overrode the seafloor, resulting in sediment mixing and complex deformation (Stages 3-4 in Figure 5b). The translation of a cohesive hanging wall across porous seafloor also may have offscraped shallow footwall strata.

6. Pore Water Geochemical Profiles

Pore water geochemical profiles collected shipboard at Site U1518 (Saffer et al., 2019; Solomon et al., 2018) provide further support for seafloor overthrusting. Near-seafloor redox reactions (Mn- and Fe-reduction, SO_4-reduction, methanogenesis, anaerobic oxidation of methane, i.e., AOM) are largely dependent on reactive organic matter concentrations and are the dominant control on pore water solute profiles in the upper ~50-100 m in continental margin sediments worldwide. Thus, duplication of seafloor sections, even those originating in different places, should produce a repetition of pore water profiles of metabolic products associated with this early diagenesis of organic matter (e.g. NH_4, PO_4, alkalinity) across the fault.

The rates of ammonium (NH_4) and phosphate (PO_4) production will be the highest in the upper ~50 m of the sediment column due to the reactivity of organic matter (e.g. Middelburg, 1989; Wallmann et al., 2006). NH_4 and PO_4 concentrations typically decrease with depth below this zone, due to decrease in organic matter degradation rates, solute diffusion, authigenic mineral precipitation, ongoing microbial activity, and adsorption. These patterns are observed in the hanging wall at Site U1518; pore water NH_4 and PO_4 concentration profiles (Figure 6) clearly reflect characteristic organic matter degradation near the present seafloor. Ammonium concentrations increase with depth to a hanging wall maximum at 71 mbsf, then decrease towards the base of the hanging wall. Phosphate concentrations also increase from seawater value near the seafloor to a peak at 21 mbsf, then decrease sharply to 58 mbsf, and remain relatively constant to the top of the Pāpaku fault. Within the footwall, ammonium and phosphate concentration profiles show similar trends as observed in the upper hanging wall; concentrations increase with depth beneath the fault zone, and then decrease to the base of the hole. The sharp increases in NH_4 and PO_4 concentrations below the fault zone are consistent with recent underthrusting of the seafloor.

352 The solute profiles across the Pāpaku fault are similar to those across Sites 1040 and 1043
353 along the Costa Rica margin drilled during ODP Leg 170, where complete underthrusting of the
354 incoming seafloor sediments beneath the lower slope wedge preserved near-seafloor signatures
355 of NH_4 and PO_4 below the deollement (e.g., Kimura et al., 1997; Tobin et al., 2001). If the
356 Pāpaku hanging wall was emplaced directly on top of the seafloor, then NH_4 and PO_4
357 concentrations also should preserve bottom water values (close to zero) immediately below the
358 fault zone, and sulfate should be enriched in the upper ~10 m of the footwall (Saffer et al., 2019).
359 Instead, we see that SO_4 is depleted and NH_4 and PO_4 concentrations are well above their
360 seawater values. This disparity in concentrations at the seafloor and top of footwall may indicate
361 that the shallowest footwall sediments were scraped off during hanging wall overthrusting,
362 although alternative explanations exist.
363 The downhole trends in Cl and Li concentrations further confirm overthrusting, and provide
364 preliminary estimates of the timing of hanging wall emplacement. Both Cl and Li concentrations
365 should increase with depth below the seafloor at Site U1518 due to shallow sediment diagenesis.
366 Immediately below the fault zone, Li concentrations step down to approximately half the
367 concentration at the base of the hanging wall, and then increase with depth, mimicking the
368 profile at the top of the hanging wall. Cl concentrations, however, exhibit a more complicated
369 pattern. Relatively high Cl concentrations occur at the base of the hanging wall due to authigenic
370 hydrous aluminosilicate formation (Saffer et al., 2019). Concentrations then decrease linearly to
371 near-seawater values just below the subsidiary fault zone. The peak in Cl concentrations seen in
372 the hanging wall at ~75 mbsf, however, is missing in the footwall trend. Its absence could be due
373 to the removal of the shallowest footwall sediments during overthrusting, or to partial removal of
374 the shallow hanging wall. More importantly, the persistence of the decreasing linear gradient in

Cl concentrations across the fault zone indicates relatively recent superposition of the hanging wall onto the footwall along the Pāpaku fault at Site U1518. Although dependent on poorly constrained boundary conditions, preliminary advection-diffusion modeling of the Cl profile indicates that underthrusting of Site U1518 occurred within the last 100 kyr, possibly as recent as 50 kyr (Solomon et al., 2018). Again, this scenario is similar to that interpreted near the deformation front of the Costa Rica margin, where the steep diffusional gradient in chloride across the plate boundary at ODP Site 1040, 1.6 km from the deformation front, is attributed to seafloor overthrusting ~17 kyr ago (e.g. Kimura et al., 1997; Saffer and Screaton, 2003; Solomon and Kastner, 2012).

In contrast to many other fault zones that have been drilled at subduction zones, no chemical anomalies occur within the Pāpaku fault zone that indicate advection of deeper-sourced fluids along the fault at Site U1518. The Pāpaku fault is interpreted to connect with the plate boundary landward of Site U1518, and thermal models show that subducted sediments at the interpreted depths are within the temperature range for mineral dehydration reactions (Antriasian et al., 2019). However, we do not observe the low Cl concentrations and elevated Li and B concentrations that are characteristic of fluid-rock reactions at these temperatures, as at other subduction zones (Kastner et al., 1991, 2006; You et al., 1995; Spivack et al., 2002; Hensen et al., 2004). These reactions may be occurring at depth, and advecting along deeper reaches of the Pāpaku fault, but lack a pathway to the seafloor along the shallow fault zone. Furthermore, the preservation of a diffusional gradient for Cl within the shallow footwall below the Pāpaku fault suggests little to no upward drainage of footwall fluids into the fault zone at Site U1518 (Solomon et al., 2018; Saffer et al., 2019). Thus, we interpret that the Pāpaku fault is a low

permeability zone that prevents drainage of the footwall, consistent with interpretations based on seismic velocities and LWD data (Gray et al., 2019; Cook et al., 2020).

7. Discussion

7.1 What Causes Seafloor Overthrusting at Subduction Margins?

At Site U1518, the primary strand of the Pāpaku fault zone defines a distinct structural boundary and stratigraphic age inversion, juxtaposing comparatively cohesive but highly fractured hanging wall rocks upon a more porous footwall section, separated by a zone of intense ductilely deformed sediments. Overthrusting of the cohesive hanging wall onto pre-existing porous seafloor explains the contrasting properties and structural histories of the two domains (Figure 5). Pore water chemical profiles confirm this interpretation (Figure 6), suggest that overthrusting was relatively recent, and record little to no signal of fluid flow along or across the fault zone.

This is only the second example of seafloor overthrusting at subduction zones documented by ocean drilling, and compares with the Costa Rica margin where the frontal wedge rides out over incoming soft sediments (Tobin et al., 2001). The two examples of seafloor overthrusting provide interesting similarities and differences. In both settings, overthrusting of more cohesive hanging wall onto and over weak porous seafloor resulted in intensely ductilely deformed sediments, although at Costa Rica the fault rocks derived from the hanging wall (Vannucchi and Tobin, 2000), rather than from the footwall as along the Pāpaku fault. Interestingly, along the Costa Rica margin, the overthrusting horizon lies along the basal décollement, which defines a planar horizon separating the overriding plate from the incoming sediments (Tobin et al., 2001).

In contrast, the locus of deformation at the Hikurangi margin is a splay fault that diverged from the megathrust and ramped through and onto the trench sediments. Thus, an essential question is why displacement along the Pāpaku fault was so large that it ramped through the entire sedimentary section and caused the hanging wall to override seafloor an additional ~3 km?

Seismic profile 05CM-04 offers little insight into the origin of the Pāpaku fault, which is interpreted to splay downdip as it approaches the megathrust fault (Figure 1c). Such large offset faults may result from variations in mechanical properties or stress conditions (e.g., Gutscher et al., 1996), but also from incoming seafloor topography. For example, seamounts and subducting plate roughness have been shown to interact with subduction forearcs in other settings (Bangs et al., 2006; Dominguez et al., 2007), and appear to influence fault locations, offsets, and longevity by deflecting deformation away from the decollement horizon. Importantly, previous studies of the northern Hikurangi margin suggest the presence of subducted seamounts beneath the forearc, recognizable from pronounced magnetic anomalies (e.g., Barker et al., 2018) and high reflectivity zones in seismic profiles attributed to porous sediments flanking buried seamounts (Bell et al., 2010). Thus we explore the potential of seamount interactions to impact the Pāpaku fault.

Numerical simulations by Morgan and Bangs (2017) clarify the consequences of seamount-forearc interactions along accretionary margins with relatively thick incoming sedimentary sections. These models demonstrate that splay faults initiate along the leading flank of a subducting seamount and propagate into the overlying sediments. Depending on the height of the seamount and the internal strength of the sedimentary section, the splay fault may ramp through the entire section to glide along the seafloor as interpreted at Hikurangi, or it can occupy an internal weak horizon to create a secondary décollement as interpreted for the Nankai margin

443 (Moore et al., 2009). If the Pāpaku fault formed in association with a seamount not visible in our
444 seismic profile, these models suggest that the seamount height is similar to the trench fill
445 thickness. Significantly, seamount-guided splay faults can accommodate disproportionately high
446 displacements (Morgan and Bangs, 2017) consistent with our interpretations for the Pāpaku fault,
447 which potentially served as the active plate boundary for a period of time.
448
449 *7.2. Mechanical and Hydraulic Consequences of Seafloor Overthrusting*
450 The intense ductile deformation documented within the Pāpaku fault at Site U1518 appears
451 to correlate with restricted advective flow from the footwall. Along the Costa Rica margin,
452 across-fault fluid flow also is significantly reduced (Tobin et al., 2001). In both settings, a
453 potential control on across-fault flow is the presence of an extensive ductilely deformed layer
454 within the fault zone. Typically fault zones cored at subduction zones are characterized by
455 abundant brittle faults, brecciation, and occasionally scaly fabrics in clay-rich materials (e.g.,
456 Lundberg and Moore, 1986; Moore et al., 2001; Kirkpatrick et al., 2014). Pervasive fracturing
457 within and adjacent to such fault zones creates important fluid conduits, recorded by
458 geochemical pore fluid anomalies that indicate the passage of deeply sourced fluids (Kastner et
459 al., 1991, 2006, 2014; You et al., 1995; Spivack et al., 2002; Hensen et al., 2004). However,
460 there is little evidence for such flow at Site U1518. The absence of active fluid flow in the
461 Pāpaku fault could be due to the lack of significant fracture permeability adjacent to the fault,
462 which may be incompatible with ongoing ductile shearing. Even pre-existing fractures in the
463 hanging wall, inherited from earlier stages of evolution of the Pāpaku fault system, are
464 predominantly filled or sealed (Savage et al., 2021), further restricting present-day fluid flow.

Ductile deformation has been shown to restrict fluid flow in fault zones elsewhere. "Clay smear" is mechanically generated clay gouge that develops along normal faults in layered sedimentary sequences, creating a fault seal in petroleum reservoirs (e.g., Vrolijik et al., 2016 and references therein). The most effective fault seals are characterized by tabular, well-mixed clay-rich lithologies that deformed by porous granular flow, commonly exhibiting planar flow-banding and local injection features, similar to the Pāpaku fault. Importantly, to serve as seals, these domains must be laterally continuous and not breached, e.g., by fracturing. The character and extent of clay smear depends on the abundance of clay in the strata, the thicknesses of the involved lithologies, and mechanical conditions (Vrolijk et al., 2016). Although clay content within the Pāpaku fault sediments only approaches ~50% by weight of total bulk sediment (Underwood, 2021), the thickness and continuity of the ductilely deformed zone within the main fault zone appears capable of restricting across-fault fluid flow, with significant implications for the mechanical conditions along the Pāpaku fault.

Figure 7 shows a hypothetical evolution of fault strength with displacement for the Pāpaku fault zone, mapped to the deformation stages shown in Figure 5. During fault initiation (Stage 1) and displacement along the thrust ramp (Stage 2), deformation was concentrated within the consolidated incoming sediments, with off-fault damage symmetrically distributed in both hanging wall and footwall (Figure 5b). Fault strength would have evolved due to strain localization and off-fault deformation, with peak strength and post-failure sliding strength defined by mechanical properties and pore fluid pressures (e.g., Moore and Byrne, 1987). However, emplacement of stronger consolidated and deformed hanging wall upon a more porous footwall flat (Stage 3 and beyond) caused fault-related deformation to migrate from the strong hanging wall into the weaker footwall. Thus, from the point of emergence onto the seafloor flat,

488 the hanging wall became a largely passive element of the system, gliding along a weaker fault
489 zone that coincided with the former seafloor. From this point on, fault strength was defined by
490 the effective shear strength of the more porous seafloor sediments, primarily governed by
491 sediment porosity and pore fluid pressures (Muir Wood, 1991). The shear stress acting on the
492 hanging wall decreased below its critical failure stress, reducing the likelihood of further fault-
493 related brittle deformation as the hanging wall slid passively on the seafloor fault, although
494 brittle structures inherited during fault initiation and folding would have been preserved.

495 The footwall at the location of Site U1518 experienced a very different mechanical
496 evolution (Figure 7). The earliest stages were characterized by burial and vertical consolidation
497 prior to incorporation into the fault zone. This is indicated by the progressive increase in shear
498 stress (Stages 1-2) that tracks decreasing porosity in the absence of shear strain (Muir Wood,
499 1991). As the hanging wall approached (Stage 3), the footwall may have felt its effects, and then
500 the superposition of the hanging wall upon the local footwall in Stage 4 fully mobilized the top
501 of the footwall in shear. Fault slip was transferred away from the hanging wall onto the top of the
502 footwall. For simplicity, effective shear stress is shown as constant with increasing shear strain
503 (black arrow), although it likely fluctuated in response to pore pressure changes or additional
504 tectonic loading. Alternatively, further consolidation of the fault zone could strengthen the fault
505 over time (gray arrow), possibly causing the locus of shear strain to migrate deeper into the
506 footwall.

507 The steps up in porosities across the main and subsidiary faults preserved at Site U1518
508 (Figure 2) suggest that the footwall has not fully consolidated under the additional load of the
509 overthrust hanging wall, and thus may still support excess pore pressures (e.g., Gray et al, 2019;
510 Cook et al., 2020). This is further supported by the lack of evidence for fluid advection at the

drill site in the solute profiles (Figure 6), and deformation experiments on representative footwall sediments (French and Morgan, 2020) that suggest pore pressure ratios as high as 0.5-0.9 of lithostatic within the fault zone. Sheared clay-rich sediments tend to have significantly lower permeabilities than their unsheared analogs (Takahashi, 2003; Cuisiat and Skurtveit, 2010), decreasing with shear strain (Ikari and Saffer, 2012). Furthermore, the intensity of ductile deformation within the Pāpaku fault zone, apparent lateral continuity of the planar flow fabric, and the comparatively minor overprint of sealed fractures and faults (Savage et al., 2021), suggest that the in-situ Pāpaku fault zone does not host abundant open fractures, at least where penetrated at Site U1518. LWD evidence for conductive fractures and macroscale deformation within the fault zone at Site U1518 are similarly sparse, except near the top of the primary fault strand (Cook et al., 2020). Thus, the comparative coherence of the fault zone and the thick continuous package of intensely sheared clay-rich sediments may define a laterally extensive fault seal that resists significant fault-normal fluid flow, at least since overthrusting occurred. This configuration has preserved excess pore pressures within the footwall and fault zone, resulting in low fault strengths along the Pāpaku fault that enable large displacements and enduring activity. Although it is still unclear how local overpressures in this setting may impact conditions along the megathrust fault, if similar low permeability structures occur elsewhere along the margin, they could enable regionally high pore fluid pressures that favor the occurrence of SSEs on the Hikurangi megathrust fault.

8. Conclusions

Predominantly ductile deformation within the large-offset Pāpaku fault at Hikurangi subduction margin Site U1518 resulted from overthrusting of a consolidated hanging wall upon a footwall composed of high porosity, previously unburied sediments at the seafloor. Overthrusting may have been associated with a subducting seamount located down-dip of the fault. The juxtaposition of the strong hanging wall upon a weak footwall caused fault-related deformation to migrate from the hanging wall onto the weaker seafloor interface below, resulting in locally intense ductile deformation, accompanied by sediment fluidization and injection. Duplication of downhole trends in pore water solute profiles across the Pāpaku fault at Site U1518 confirm the seafloor overthrusting model. The preservation of typical near-seafloor, early diagenetic profiles below the fault indicate relatively recent overthrusting, possibly ~50-100 kya (Saffer et al., 2019; Solomon et al., 2018), and demonstrate little to no advective fluid flow either along or across the fault. The intense ductile deformation along the fault zone is interpreted to have produced a thick continuous layer of low permeability fault rocks resistant to fluid flow, which preserves high pore pressures within the underthrust sediments and fault zone (French and Morgan, 2020; Gray et al., 2019; Cook et al., 2020). In combination, the extensive ductile deformation, apparently low fracture permeability, and enhanced pore pressures along the fault, likely define a fault seal that prevents fluid flow in this location. This distinctive structural, mechanical, and hydraulic configuration defines a significant tectonic feature along the frontal Northern Hikurangi Margin. If similar low permeability structures occur elsewhere along the margin, they may preserve high pore fluid pressures that enable SSEs on the Hikurangi megathrust fault.

Acknowledgements

This research used samples and data provided by the International Ocean Discovery Program. We thank the staff and scientists onboard the JOIDES Resolution during Expeditions 372 and 375 for valuable discussions and support. This work was funded by USSSP-IODP Subaward 66B(GG009393) of NSF Award OCE1450528 to Morgan and NSF Award OCE1753617 to Solomon.

562 **References**
563
564 Antriasian, A., Harris, R.N., Trehu, A.M., Henrys, S.A., Phrampus, B.J., Lauer, R., Gorman,
565 A.R., Pecher, I.A., and Barker, D., 2019, Therman regim of the Northern Hikurangi margin,
566 New Zealand, Geophysical Journal International, 216, 1177-1190, doi: 10.1093/gji/ggy450.
567 Bangs, N.L.B., Gulick, S.P.S., and Shipley, T.H., 2006, Seamount subduction erosion in the
568 Nankai Trough and its potential impact on the seismogenic zone: Geology, v. 34, p. 701–
569 704, doi: 10.1130 /G22451 .1.
570 Barker, D. H. N., Henrys, S., Caratori Tontini, F., Barnes, P. M., Bassett, D., Todd, E., and
571 Wallace, L., 2018, Geophysical constraints on the relationship between seamount
572 subduction, slow slip and tremor at the north Hikurangi subduction zone, New Zealand,
573 Geophys. Res. Lett. doi.org/10.1029/2018GL080259.
574 Barnes, P.M., Wallace, L.M., Saffer, D.M., Pecher, I.A., Petronotis, K.E., LeVay, L.J., and the
575 Expedition 372/375 Scientists, 2019, Site U1520. In Wallace, L.M., Saffer, D.M., Barnes,
576 P.M., Pecher, I.A., Petronotis, K.E., LeVay, L.J., and the Expedition 372/375 Scientists,
577 Hikurangi Subduction Margin Coring, Logging, and Observatories. Proceedings of the
578 International Ocean Discovery Program, 372B/375: College Station, TX .
579 Barnes, P.M., Wallace, L.M., Saffer, D.M., Bell, R.E., Underwood, M.B., Fagereng, A.,
580 Meneghini, F., Savage, H.M., Rabinowitz, H.S., Morgan, J.K., Kitajima, H., Kutterolf, S.,
581 Hashimoto, Y., Engelmann de Oliveira, C.H., Noda, A., Crundwell, M.P., Shepherd, C.L.,
582 Woodhouse, A.D., Harris, R.N., Wang, M., Henrys, S., Barker, D.H.N., Petronotis, K.E.,
583 Bourlange, S.M., Clennell, M.B., Cook, A.E., Dugan, B.E., Elger, J., Fulton, P.M., Gamboa,
584 D., Greve, A., Han, S., Hüpers, A., Ikari, M.J., Ito, Y., Young Kim, G., Koge, H., Lee, H.,
585 Li, X., Luo, M., Malie, P.R., Moore, G.F., Mountjoy, J.J., McNamara, D.D., Paganoni, M.,
586 Screaton, E.J., Shankar, U., Shreedharan, S., Solomon, E.A., Wang, X., Wu, H-Y., Pecher,
587 I.A., LeVay, L.J., and; IODP Expedition 372 Scientists, 2020, Slow slip source
588 characterized by lithological and geometric heterogeneity, Science Advances 6 (13),
589 eaay3314, DOI: 10.1126/sciadv.aay3314.
590 Boyer, S. E. and Elliott, D. 1982. Thrust systems. American Association of Petroleum
591 Geologists, 66, 1196–1230.
592 Collot, J.-Y., Lewis, K., Lamarche, G., and Lallemand, S., 2001, The giant Ruatoria debris
593 avalanche on the northern Hikurangi margin, New Zealand, result of oblique seamount
594 subduction. J. Geophys. Res. 106, 19271–19297.
595 Cook, A.E., Paganoni, M., Clennell, M.B., McNamara, D.D., Nole, M., Wang, X., Han, S., Bell,
596 R.E., Solomon, E.A., Saffer, D.M., Barnes, P.M., Pecher, I.A., Wallace, L.M., LeVay, L.J.,
597 and Petronotis, K.E., 2020, Physical properties and gas hydrate at a near-seafloor thrust
598 fault, Hikurangi Margin, New Zealand. Geophysical Research Letters. 47, e2020GL088474.
599 https://doi.org/10.1029/2020GL088474.
600 Cosgrove, J.W., 2015, The association of folds and fractures and the link between folding,
601 fracturing and fluid flow during the evolution of a fold–thrust belt: a brief review,
602 Geological Society, London, Special Publications, 421, 41-68,
603 https://doi.org/10.1144/SP421.11.
604 Crundwell, M.P., and Woodhouse, A.D., 2022, Biostratigraphically constrained chronology of
605 Quaternary rocks from IODP Expeditions 372 and 375, Hikurangi margin, New Zealand,
606 New Zealand Journal of Geology and Geophysics, in review.

607 Cuisiat, F., Skurtveit, E., 2010. An experimental investigation of the development and
608 permeability of clay smears along faults in uncemented sediments. J. Struct. Geol. 32, 1850-
609 1863.
610 Davy, R. G., Frahm, L., Bell, R., Arai, R., Barker, D. H. N., Henrys, S., et al., 2021, Generating
611 high-fidelity reflection images directly from full-waveform inversion: Hikurangi subduction
612 zone case study. Geophysical Research Letters, 48, e2021GL094981.
613 https://doi.org/10.1029/2021GL094981.
614 Dominguez, S., Malavieille, J., and Lallemand, S.E., 2000, Deformation of accretionary wedges
615 in response to seamount subduction: Insights from sandbox experiments: Tectonics, v. 19, p.
616 182–196, doi: 10 .1029 /1999TC900055.
617 Doser, D., and Webb, T.H., 2003, Source parameters of large historical (1917 to 1961)
618 earthquakes, North Island, New Zealand. Geophys. J. Int. 152, 795–832.
619 Fagereng, Å., Diener, J.F., Ellis, S. and Remitti, F., 2018. Fluid-related deformation processes at
620 the up-and down-dip limits of the subduction thrust seismogenic zone: What do the rocks
621 tell us? Geol. Soc. Am. Spec. Paper 534, p. 187-215.
622 Fagereng, A., Savage, H.M., Morgan, J.K., Wang, M., Meneghini, F., Barnes, P.M., Bell, R.,
623 Kitajima, H., McNamara, D.D., Saffer, D.M.,Wallace, L.M., Petronotis, K., LeVay, L., and
624 the IODP Expedition 372/375 Scientists*, 2019, Mixed deformation styles observed on a
625 shallow subduction thrust, Hikurangi margin, New Zealand, Geology, v. 47, p. 1–5, https://
626 doi .org /10 .1130 /G46367.1.
627 French, M. E., and Morgan, J. K., 2020, Pore fluid pressures and strength contrasts maintain
628 frontal fault activity, northern Hikurangi margin, New Zealand. Geophysical Research
629 Letters, 47, e2020GL089209. https://doi.org/10.1029/2020GL089209.
630 Gray, M., Bell, R. E., Morgan, J. V., Henrys, S., & Barker, D. H. N., 2019, Imaging the shallow
631 subsurface structure of the North Hikurangi Subduction Zone, New Zealand, using 2-D full-
632 waveform inversion. Journal of Geophysical Research: Solid Earth, 124, 9049–9074.
633 https://doi.org/10.1029/2019JB017793.
634 Greve, A., Kars, M., Zerbst, L., Stipp, M., and Hashimoto, Y., 2020, Strain partitioning across a
635 subduction thrust fault near the deformation front of the Hikurangi subduction margin, New
636 Zealand: A magnetic fabric study on IODP Expedition 375 Site U1518, Earth Planet. Sci.
637 Lett., 542, 116322, https://doi.org/10.1016/j.epsl.2020.116322.
638 Hensen, C., Wallmann, K., Schmidt, M., Ranero, C., Suess, E. 2004. Fluid expulsion related to
639 mud extrusion off Costa Rica—a window to the subducting slab. *Geology* 32(2):201–4.
640 Ikari, M.J., and Saffer, D.M., 2012, Permeability contrasts between sheared and normally
641 consolidated sediments in the Nankai accretionary prism, Marine Geology, 295-298, 1-13.
642 Kastner, M., Elderfield, H., and Martin, J.B. 1991. Fluids in convergent margins: What do we
643 know about their composition, origin, role in diagenesis and importance for oceanic
644 chemical fluxes? *Philos. Trans. R. Soc. Lond. Ser. A* 335:243–59.
645 Kastner, M., Solomon, E.A., Harris, R.N., and Torres, M.E., 2014, 7. Fluid origins, thermal
646 regimes, and fluid and solute fluxes in the forearc of subduction zones, in Developments in
647 Marine Geology, 7, 671-733, http://dx.doi.org/10.1016/B978-0-444-62617-2.00022-0.
648 Kastner, M., Solomon, E.A., Wei, W., Chan, L.H., and Saether, O.M., 2006. Chemical and
649 isotopic composition of pore fluids and sediments across the Middle America Trench,
650 offshore Costa Rica, in Morris J., Villinger H., and Klaus A. (Eds.), Proceedings ODP,
651 Scientific Results Leg 205: College Station, TX (Ocean Drilling Program), 1–21.
652 doi:10.2973/odp.proc.sr.205.208.2006.

Kimura, G., Silver, E., Blum, P., and shipboard scientific party. 1997. *Proc. Ocean Drill. Program Initial Rep.*, Vol. 170. College Station, TX: Ocean Drill. Program. 554 pp.

Kirkpatrick, J.D., Rowe, C.D., Ujiie, K., Moore, J.C., Regalla, C., Remitti, F., Toy, V., Wolfson-Schweh, M., Kameda, J., Bose, S., and Chester, F.M., 2015, Structure and lithology of the Japan Trench subduction plate boundary fault, Tectonics, 34, 53–69, doi:10.1002/2014TC003695.

Lay,T., Kanamori, H., Ammon, C.J., Nettles, M., Ward, S.N., Aster, R.C., Beck, S.L., Bilek, S.L., Brudzinski, M.R., Butler, R., DeShon, H.R., Ekström, G., Satake, K., Sipkin, S., 2005, The great Sumatra-Andaman earthquake of 26 December 2004, Science, 308, 1127-1133.

Lundberg, N., and Moore, J.C., 1986, Macroscopic structural features in Deep Sea Drilling Project cores from forearc regions, in *Structural Fabrics in Deep Sea Drilling Project Cores from Forearcs,* edited by J.C. Moore, Mem. Geol. Soc. Am., 166, 13-44.

Martin, K.M., S.P.S. Gulick, N.L.B. Bangs, G.F. Moore, J. Ashi, J.-O. Park, S. Kuramoto, and A. Taira (2010), Possible strain partitioning structure between the Kumano forearc basin and the slope of the Nankai Trough accretionary prism, Geochem. Geophys. Geosyst., 11, Q0AD02, doi:10.1029/2009GC002668.

Meneghini, F., and Moore, J.C., 2007, Deformation and hydrofracture in a subduction thrust at seismogenic depths: The Rodeo Cove thrust zone, Marin Headlands, California, GSA Bulletin, 119, 174-183. https://doi.org/10.1130/B25807.1.

Middelburg, J.J., 1989. A simple model for organic matter decomposition in marine sediments, Geochim. Cosmochim. Acta, 53, 1577-1581.

Morgan, J.K., and Bangs, N., 2017, Recognizing seamount - forearc collisions at accretionary margins: Insights from discrete numerical simulations, Geology, 45:7, 635-638, DOI: 10.1130/G38923.1.

Moore, G.F., Bangs, N.L., Taira, A., Kuramoto, S., Pangborn, E., and Tobin, H.J., 2007, Three-dimensional splay fault geometry and implications for tsunami generation, Science, 318, 1128-1131.

Moore, G.F., et al., 2009, Structural and seismic stratigraphic framework of the NanTroSEIZE Stage 1 transect, in Kinoshita, M., et al., Proceedings of Integrated Ocean Drilling Program, Volume 314/315/316: Washington, D.C., Integrated Ocean Drilling Program Management International, Inc., 46 p., doi: 10 .2204 /iodp .proc .314315316.102 .2009.

Moore, G. F., Taira, A., Klaus, A., Becker, L., Boeckel, Babette, Cragg, Barry A., Dean, A., Fergusson, C.L., Henry, P., Hirano, S., Hisamitsu, T., Hunze, S., Kastner, M., Maltman, A.J., Morgan, J.K., Murakama, Y., Saffer, D.M., Sanchez-Gomez, M., Screaton, E.J., Smith, D.C., Spivack, A.J., Steurer, J., Tobin, H.J., Ujiie, K., Underwood, M.B., and Wilson, M., 2001, New insights into deformation and fluid flow processes in the Nankai Trough accretionary prism: Results of Ocean Drilling Program Leg 190, Geochem. Geophys. Geosyst., 2, doi:10.129/2001GC000166.

Moore, J.C., and Byrne, T. 1987, Thickening of fault zones: A mechanism of melange formation in accreting sediments Geology 15, 1040–1043.

Moore, G.F., Lackey, J.K., Strasser, M., and Yamashita, M., 2019, Submarine landslides on the Nankai Trough accretionary prism, American Geophysical Union Monograph 246, 247-259.

Muir Wood, D., 1991. Soil behaviour and critical state soil mechanics. Cambridge: Cambridge University, Press. pp 462. https://doi.org/10.1017/CBO9781139878272.

697 Park, J.-O., Tsuru, T., Kodaira, S., Cummins, P.R., and Kaneda, Y., 2002, Splay fault branching
698 along the Nankai subduction zone: Science, v. 297, p. 1157–1160, doi: 10 .1126 /science
699 .1074111.
700 Saffer, D.M., and Screaton, E.J., 2003. Fluid flow at the toe of convergent margins:
701 interpretation of sharp pore-water geochemical gradients, Earth Planet. Sci. Lett., 213, 261-
702 270.
703 Saffer, D.M., and Tobin, H.J., 2011, Hydrogeology and mechanics of subduction zone forearcs:
704 Fluid flow and pore pressure, Annual Review of Earth and Planetary Sciences, 39, 157-186,
705 https://doi.org/10.1146/annurev-earth-040610-133408.
706 Saffer D.M. and Wallace L.M., 2015, The frictional, hydrologic, metamorphic and thermal
707 habitat of shallow slow earthquakes, Nat. Geosci. 8, 594–600. doi:10.1038/ngeo2490.
708 Saffer, D.M., Wallace, L.M., Barnes, P.M., Pecher, I.A., Petronotis, K.E., LeVay, L.J., and the
709 Expedition 372/375 Scientists 2019, Site U1518. In Wallace, L.M., Saffer, D.M., Barnes,
710 P.M., Pecher, I.A., Petronotis, K.E., LeVay, L.J., and the Expedition 372/375 Scientists,
711 Hikurangi Subduction Margin Coring, Logging, and Observatories. Proceedings of the
712 International Ocean Discovery Program, 372B/375: College Station, TX .
713 Savage, H.M., Shreedharan, S., Fagereng, A., Morgan, J.K., Meneghini, F., Wang, M.,
714 McNamara, D.D., Wallace, L.M., Saffer, D.M., Barnes, P.M., Petronotis, K.E., LeVay, L.J.,
715 2021, Asymmetric Brittle Deformation at the Pāpaku Fault, Hikurangi Subduction Margin,
716 NZ, IODP Expedition 375, Geochemistry, Geophysics, Geosystems, 22, e2021GC009662.
717 https://doi.org/10.1029/2021GC009662
718 Savage, H. M., and Brodsky, E. E., 2011, Collateral damage: Evolution with displacement of
719 fracture distribution and secondary fault strands in fault damage zones, J. Geophys. Res.,
720 116(B3), B03405, doi:10.1029/2010jb007665.
721 Solomon, E.A., Hüpers, A., Luo, M., Malié, P., Saffer, D., Torres, M., Wallace, L., Petronotis,
722 K., Barnes, P., Pecher, I., Levay, L., and Expedition 372 and 375 Scientists, 2018,
723 Geochemical constraints on fluid-rock reactions, fluid sources, and flow pathways along the
724 IODP Expedition 375 Transect; Northern Hikurangi Margin, American Geophysical Union
725 99, Fall Meet. Suppl., Abstract T54C-07.
726 Solomon, E.A., and Kastner, M., 2012. Progressive barite dissolution in the Costa Rica forearc –
727 implications for global fluxes of Ba to the volcanic arc and mantle, Geochimica et
728 Cosmochimica Acta, 83, 110-124.
729 Spivack, A., Kastner, M., Ransom, B., 2002. Elemental and isotopic chloride geochemistry and
730 fluid flow in the Nankai Trough, Geophys. Res. Lett., 29, doi:10.1029/2001GL014122.
731 Strasser, M., G. F. Moore, G. Kimura, A. J. Kopf, M. B. Underwood, J. Guo, and E. J. Screaton
732 (2011), Slumping and mass transport deposition in the Nankai fore arc: Evidence from
733 IODP drilling and 3‐D reflection seismic data, Geochem. Geophys. Geosyst., 12,
734 Q0AD13, doi:10.1029/2010GC003431.
735 Suppe, J., 1983, Geometry and Kinematics of fault-bend folding. American Journal of Science,
736 283, 684–721.
737 Taira, A., Hill, I., Firth, J., Berner, U., Bruckmann, W. , Byrne, T., Chabernaud, T., Fisher, A.,
738 Foucher, J-P., Gamo, T., Gieskes, J., Hyndman, R., Karig, D.E., Kastner, M., Kato, Y.,
739 Lallemant, S., Lu, R., Maltman, A., Moore, G., Moran, K., Olaffson, G., Owens, W.,
740 Pickering, K., Siena, F., Taylor, E., Underwood, M., Wilkinson, C., Yamano, M., and
741 Zhang, J., 1992, Sediment deformation and hydrogeology of the Nankai Trough accretionary

prism: Synthesis of shipboard results of ODP Leg 131, Earth Planet. Sci Letters, 109, 431-450.
Takahashi, M., 2003. Permeability change during experimental fault smearing. J. Geophys. Res. 108.
Tobin, H., Vannucchi, P., and Meschede, M., 2001, Structure, inferred mechanical properties, and implications for fluid transport in the décollement zone, Costa Rica convergent margin, Geology, 29, 907-910.
Underwood, M.B., 2021, Data report: clay mineral assemblages within biocalcareous and volcaniclastic inputs to the Hikurangi subduction zone, IODP Expedition 372B/375 Sites U1520 and U1526, offshore New Zealand. In Wallace, L.M., Saffer, D.M., Barnes, P.M., Pecher, I.A., Petronotis, K.E., LeVay, L.J., and the Expedition 372/375 Scientists, Proceedings of the International Ocean Discovery Program Volume 372B/375, https://doi.org/10.14379/iodp.proc.372B375.207.2021.
Vannucchi, P., and Tobin, H., 2000, Deformation structures and implications for fluid flow at the Costa Rica convergent margin, ODP Sites 1040 and 1043, Leg 170, J. Structural Geology, 22, 1087-1103.
Vrolijk, P.J., Urai, J.L., and Ketterman, M., 2016, Clay smear: Review of mechanisms and applications, J. Structural Geology, 86, 95-152.
Wallace, L.M., Beavan, J., McCaffrey, R., Darby, D., 2004, Subduction zone coupling and tectonic block rotations in the North Island, New Zealand. J. Geophys. Res. 109, B12406.
Wallace, L.M., and Beavan, J., 2010, Diverse slow slip behavior at the Hikurangi subduction margin, New Zealand. Journal of Geophysical Research: Solid Earth, 115(B12):B12402.
Wallace, L.M., Saffer, D.M., Barnes, P.M., Pecher, I.A., Petronotis, K.E., LeVay, L.J., and the Expedition 372/375 Scientists, 2019. Hikurangi Subduction Margin Coring, Logging, and Observatories. Proceedings of the International Ocean Discovery Program, 372B/375: College Station, TX (International Ocean Discovery Program). https://doi.org/ 10.14379/ iodp.proc.372B375.2019
Wallace, L.M., Webb, S. C., Ito, Y., Mochizuki, K., Hino, R., Henrys, S.A., Schwartz, S.Y., and Sheehan, A.F., 2016, Slow slip near the trench at the Hikurangi subduction zone, New Zealand, Science 352, 701–704.
Wallmann, K., Aloisi, G., Haeckel, M., Obzhirov, A., Pavlova, G., Tischchenko, P., 2006. Kinetics of organic matter degradation, microbial methane generation, and gas hydrate formation in anoxic marine sediments, Geochim. Cosmochim. Acta, 70, 3905-3927.
You, C.F., Spivack, A.J., Gieskes, J.M., Rosenbauer, R., Bischoff, J.L., 1995. Experimental study of boron geochemistry: implications for fluid processes in subduction zones. Geochim. Cosmochim. Acta 59, 2435–2442.

Figure Captions

Figure 1. (a) Tectonic setting of the northern Hikurangi margin (bathymetry from GeoMapApp); black box shows approximate location of survey area shown in (b). (b) Bathymetry of study area showing locations of seismic line 05CM-04 (black line) and Expedition 375 drill sites (red dots). Blue box shows location of seismic profile. (c) Depth converted pre-stack time migrated seismic profile 05CM-04 (after Barker et al., 2018), showing location of Site U1518, with stratigraphic and structural interpretations modified from Barnes et al. (2020) and Davy et al. (2021). Further details of the interpretation of the Papaku fault hanging wall stratigraphy are shown in Davy et al. (2021). Seismic units (SU) are defined at IODP Site U1520 (Barnes et al., 2019).

Figure 2. Summary of core observations with depth from Site U1518. (a) Core recovery from Holes U1518E and U1518F. (b) Graphic lithology, showing lithologic units and age; key at bottom of figure. (c) Discrete sample porosity measurements (small open circles), core average values (large filled circles), and LWD neutron porosities (gray lines). (d) Bedding dips. (e) Fracture (solid squares) and fault dips (open squares). Modified after Saffer et al., (2019).

Figure 3. Synthesis of core and section observations across the main strand of the Pāpaku fault and immediately adjacent wall rocks. Key shows symbols used here. Missing core denoted by large X and unrecovered core is symbolized at the based of each core. Interpreted hanging wall (HW), main fault zone (FZ), and footwall (FW) are labeled and uniquely shaded. Locations of core photos in Figure 4 are denoted.

Figure 4. Representative core samples with locations noted on Figure 3. All intervals are from Hole 375-U1518F. Hanging wall: (a) normal fault offsets silt bed and terminates in brecciated zones (13R-1W, 46-53 cm), (b) abundant fractures cross-cut distorted sedimentary layers (13R-1A, 88-94 cm). Main fault zone: (c) variably oriented color banding at top of fault zone (13R-1A, 112-117 cm), (d) brecciated rock with discordant flow-banding (13R-2A, 28-33 cm), (e) finely laminated flow-banded mudstone with elongated clasts (13R-3W, 11-33 cm), (f) disaggregated sediment injected into adjacent cohesive rock (13R-3W, 82-88 cm), (g) distorted and truncated stacks of mudstones and silt layers cross-cut by fractures (14R-1A, 126-140 cm), (h) flow-banded unit with homogenized gray material cross-cut by normal faults (14R-2A, 34-42 cm). Footwall: (i) small injection feature (15R-1A, 18-22 cm), (j) dismembered silt beds (15R-2A, 1-7 cm), (k) silt beds distorted into recumbent fold (15R-3A, 109-112 cm), (l) mud clast with asymmetric tails in coarse flow-banding (18R-1A, 77-81 cm).

Figure 5. (a) Hypothetical kinematic reconstruction of the frontal Hikurangi margin, showing stages of evolution of the Pāpaku fault (T_2), from the initiation of Papaku fault (Stage 1), initial uplift and folding the hanging wall (Stage 2), hanging wall overthrusting and slumping (Stage 3), and juxtaposition of hanging wall and footwall at Site U1518 (Stage 4). Dotted and gray boxes show the trajectory of the hanging wall and position of the footwall, respectively. (b) and (c) Schematic deformation paths of materials within the dotted and gray boxes in (a) at each stage for the hanging wall and footwall, respectively, as they undergo contrasting deformation histories and eventually converge at Site U1518. See text for details.

Figure 6. Concentration profiles of (a) NH_4, (b) PO_4, (c) SO_4, (d) Cl, and (e) Li. Blue and red circles represent data for hanging wall and footwall samples, respectively. Open circles represent phosphate and sulfate concentrations measured by spectrophotometry and ion chromatography, respectively and closed circles measured by ICP-AES (Saffer et al., 2019). Horizontal dashed lines mark lithological unit boundaries, shaded bars locate the main and subsidiary fault zones. Vertical dotted lines indicate seawater values.

Figure 7. Hypothetical stress-strain histories of the hanging wall (no shading), and shared history of the footwall and fault zone (shaded), with Stages 1 through 4 from Figure 5 denoted for both settings. The stress and shear strain magnitudes are only representative, showing hypothesized relative magnitudes. See text for discussion.

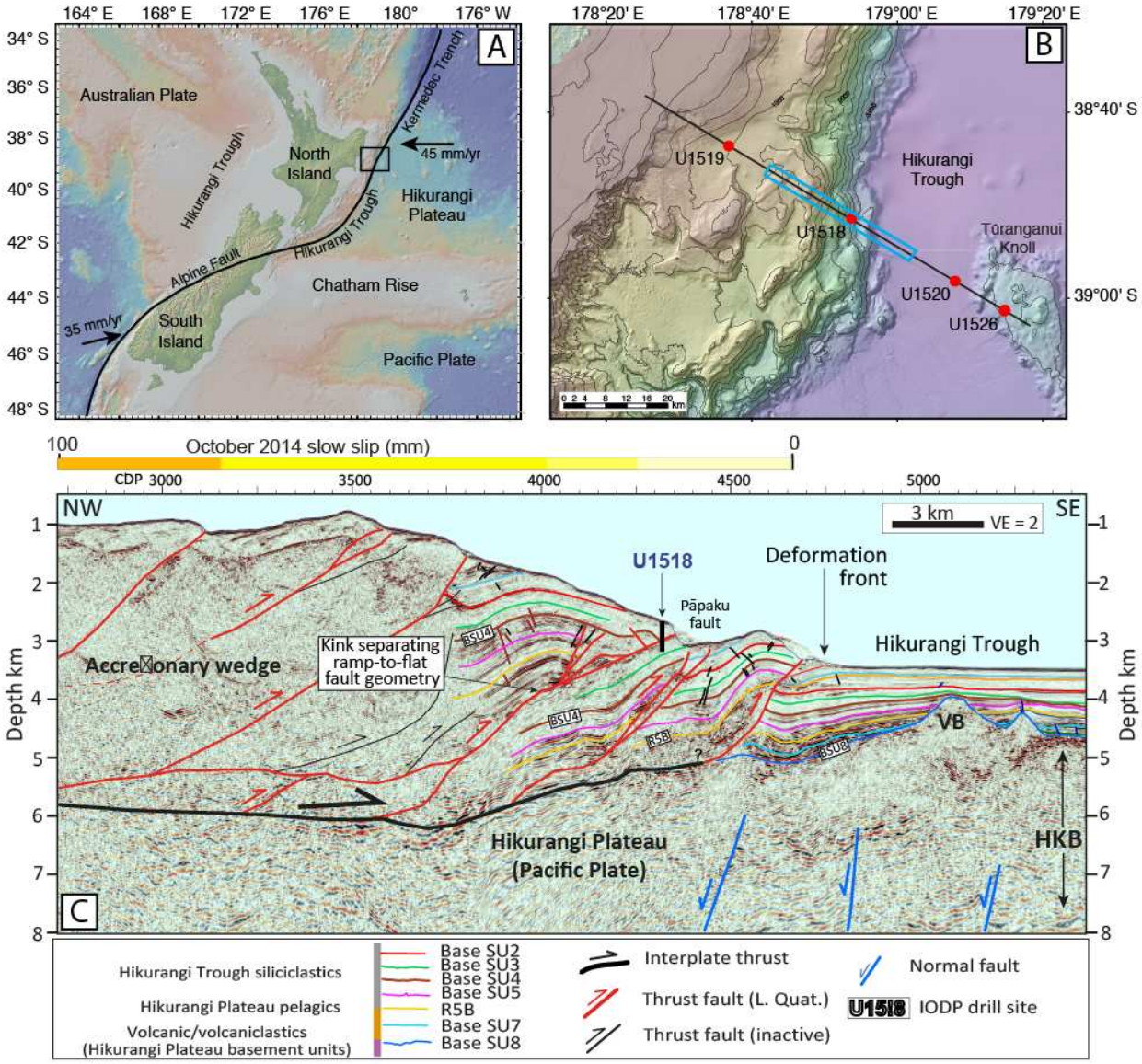
A
Australian Plate
North Island
South Island
Hikurangi Trough
Kermadec Trench
45 mm/yr
Hikurangi Plateau
Alpine Fault
Chatham Rise
35 mm/yr
Pacific Plate
B
U1519
U1518
U1520
U1526
Hikurangi Trough
Tūranganui Knoll
38°40' S
39°00' S
October 2014 slow slip (mm)
CDP 3000
3500
4000
4500
5000
NW
SE
3 km
VE = 2
U1518
Deformation front
Pāpaku fault
Hikurangi Trough
Accretionary wedge
Kink separating ramp-to-flat fault geometry
BSU4
R5B
BSU8
VB
HKB
Hikurangi Plateau (Pacific Plate)
C
Depth km
Hikurangi Trough siliciclastics
Hikurangi Plateau pelagics
Volcanic/volcaniclastics (Hikurangi Plateau basement units)
Base SU2
Base SU3
Base SU4
Base SU5
R5B
Base SU7
Base SU8
Interplate thrust
Thrust fault (L. Quat.)
Thrust fault (inactive)
Normal fault
U1518 IODP drill site

Figure 1

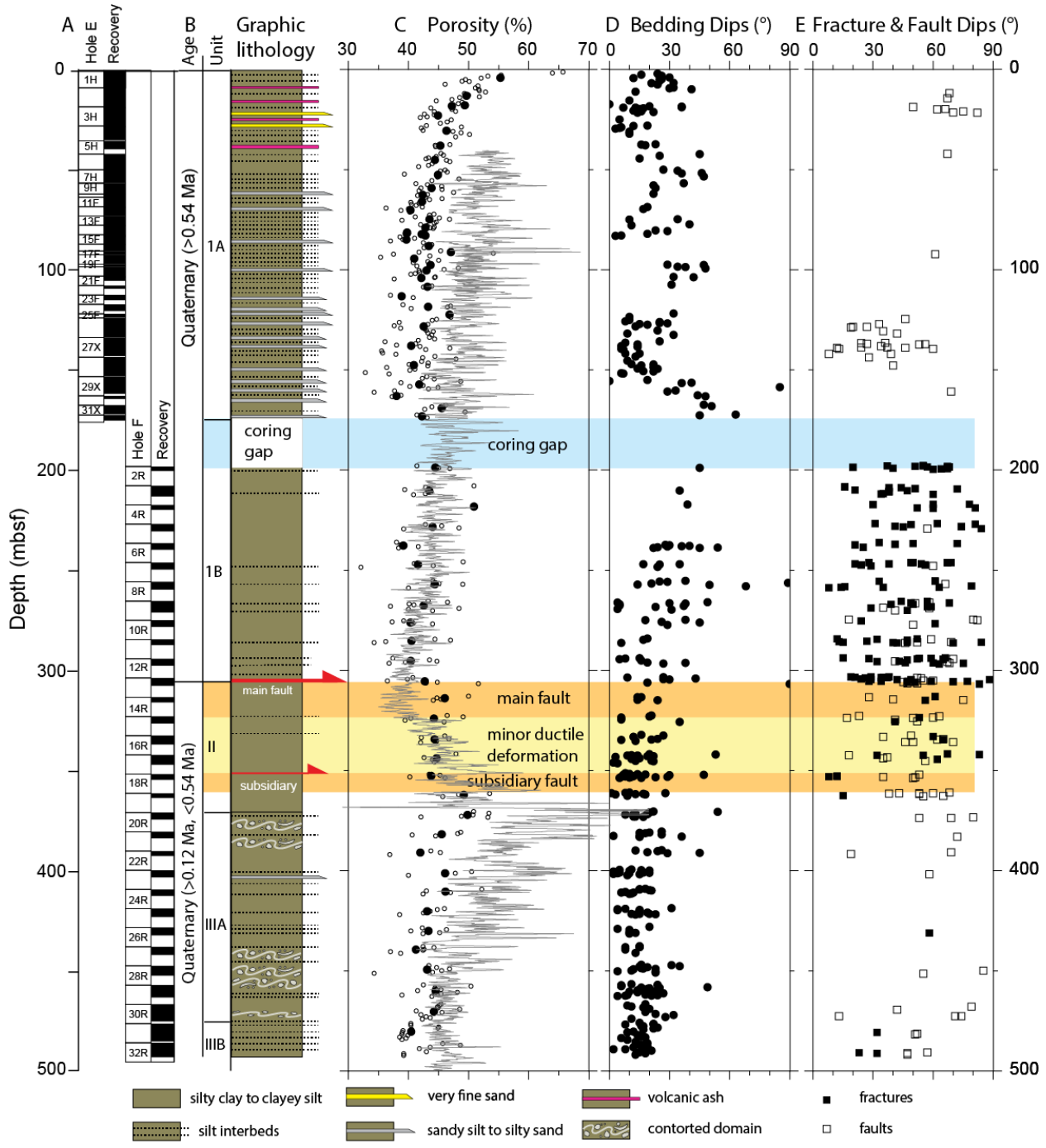
A
Hole E
Recovery
B
Age
Unit
Graphic lithology
C Porosity (%)
D Bedding Dips (°)
E Fracture & Fault Dips (°)
Depth (mbsf)
Hole F
Recovery
Quaternary (>0.54 Ma)
Quaternary (>0.12 Ma, <0.54 Ma)
1A
1B
II
IIIA
IIIB
coring gap
main fault
minor ductile deformation
subsidiary fault
silty clay to clayey silt
silt interbeds
very fine sand
sandy silt to silty sand
volcanic ash
contorted domain
fractures
faults

Figure 2

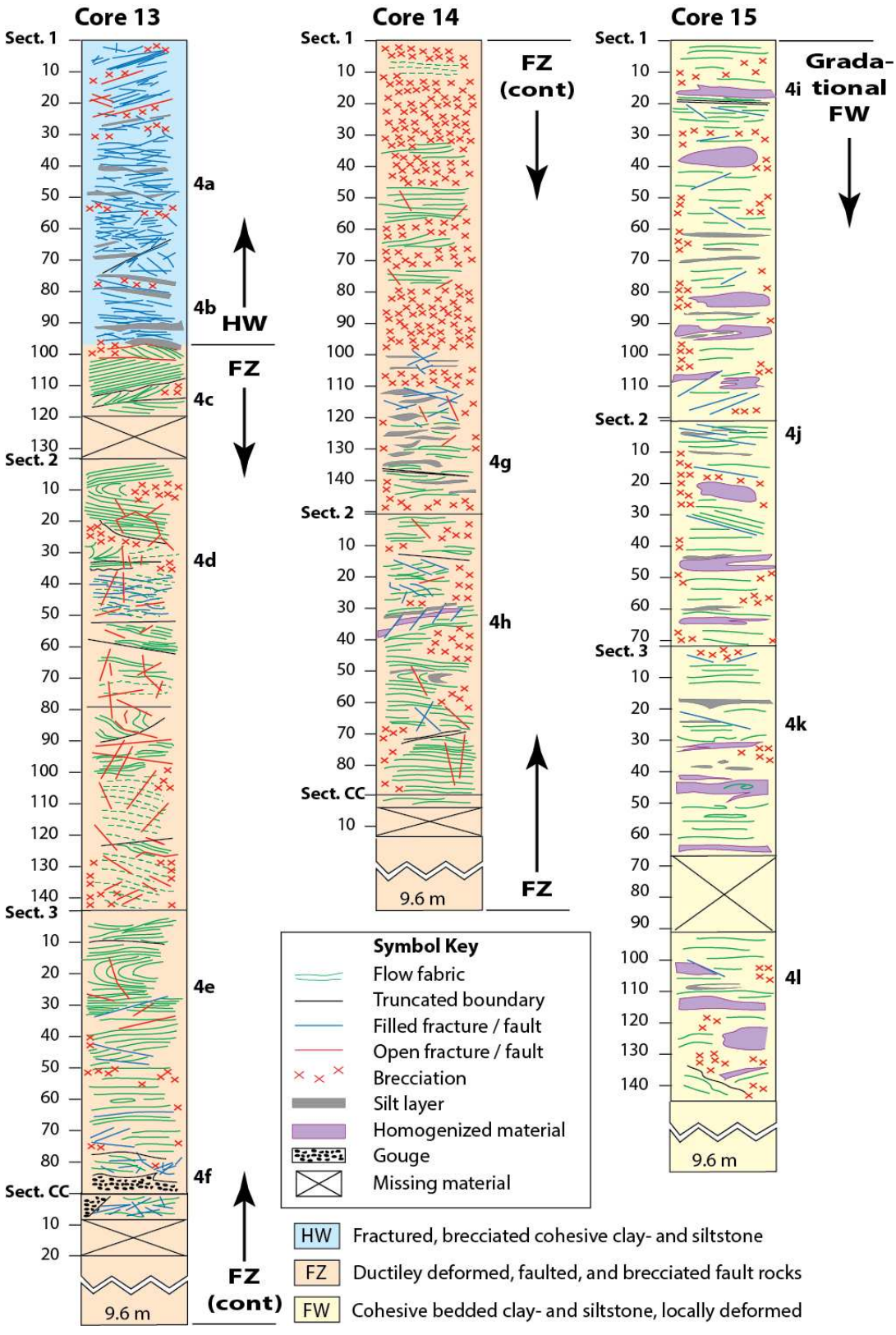
Core 13
Core 14
Core 15
Sect. 1
Sect. 2
Sect. 3
Sect. CC
4a
4b
4c
4d
4e
4f
4g
4h
4i
4j
4k
4l
HW
FZ
FZ (cont)
Grada-tional FW
9.6 m
Symbol Key
Flow fabric
Truncated boundary
Filled fracture / fault
Open fracture / fault
Brecciation
Silt layer
Homogenized material
Gouge
Missing material
HW Fractured, brecciated cohesive clay- and siltstone
FZ Ductiley deformed, faulted, and brecciated fault rocks
FW Cohesive bedded clay- and siltstone, locally deformed

Figure 3

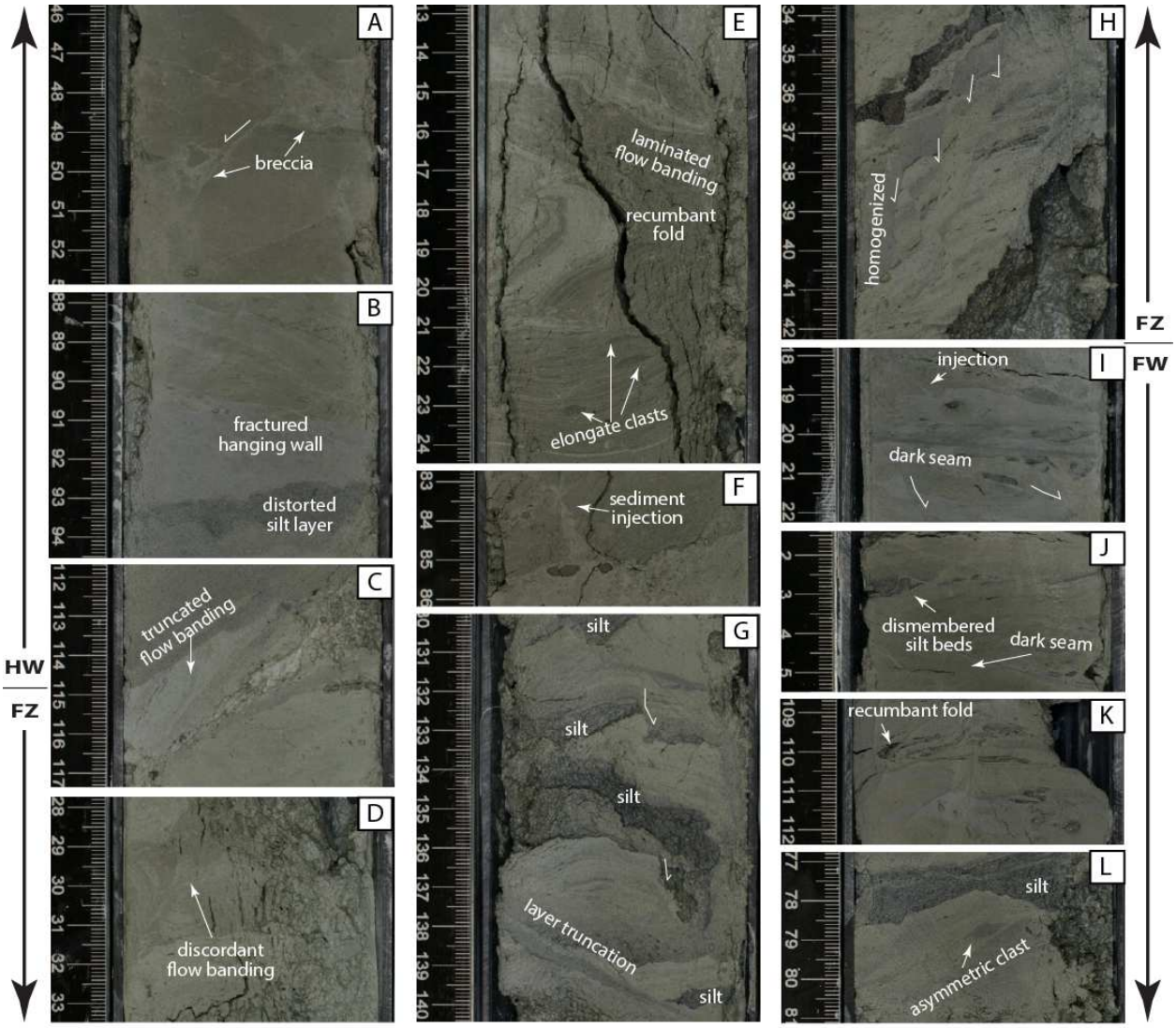

Figure 4. Representative core intervals, with locations noted on Figure 3. All intervals are from Hole 375-U1518F. Hanging wall: (a) normal fault offsets silt bed and terminates in brecciated zones (13R-1W, 46-53 cm), (b) abundant fractures cross-cut distorted sedimentary layers (13R-1A, 88-94 cm). Main fault zone: (c) variably oriented color banding at top of fault zone (13R-1A, 112-117 cm), (d) brecciated rock with discordant flow banding (13R-2A, 28-33 cm), (e) finely laminated flow banded mudstone with elongated clasts (13R-3W, 11-33 cm), (f) disaggregated sediment injected into adjacent cohesive rock (13R-3W, 82-88 cm), (g) distorted and truncated stacks of mudstones and silt layers cross-cut by fractures (14R-1A, 126-140 cm), (h) flow-banded unit with homogenized gray material cross-cut by normal faults (14R-2A, 34-42 cm). Foot wall: (i) small injection feature (15R-1A, 18-22 cm), (j) dismembered silt beds (15R-2A, 1-7 cm), (k) silt beds distorted into recumabnt fold (15R-3A, 109-112 cm), (l) mud clast with asymmetric tails in coarse flow banding (18R-1A, 77-81 cm).

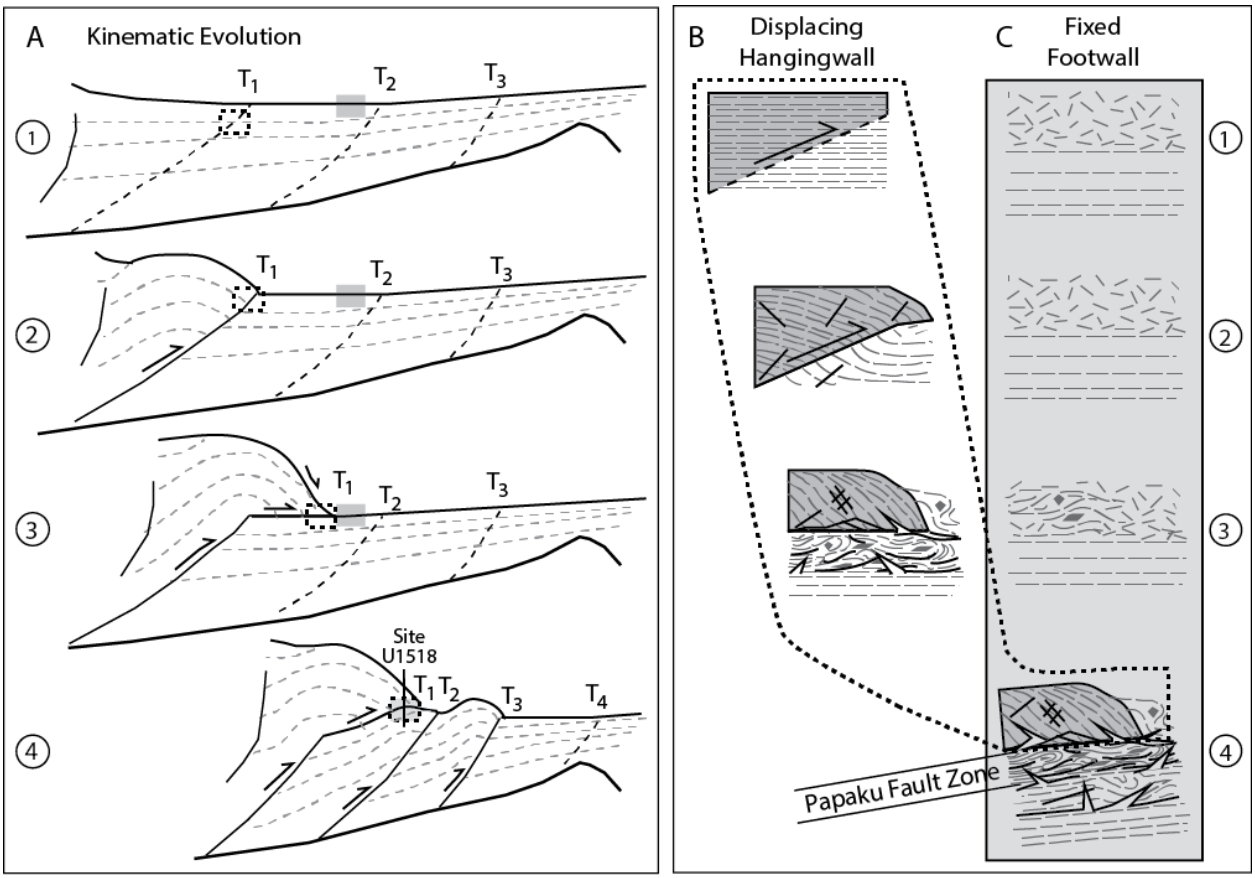

Figure 5

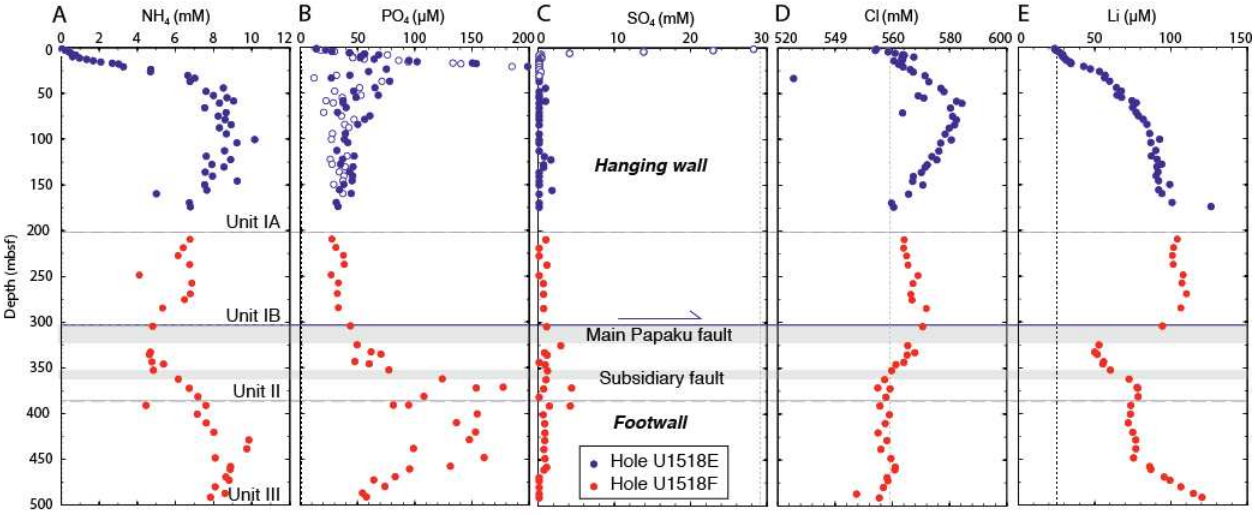

Figure 6

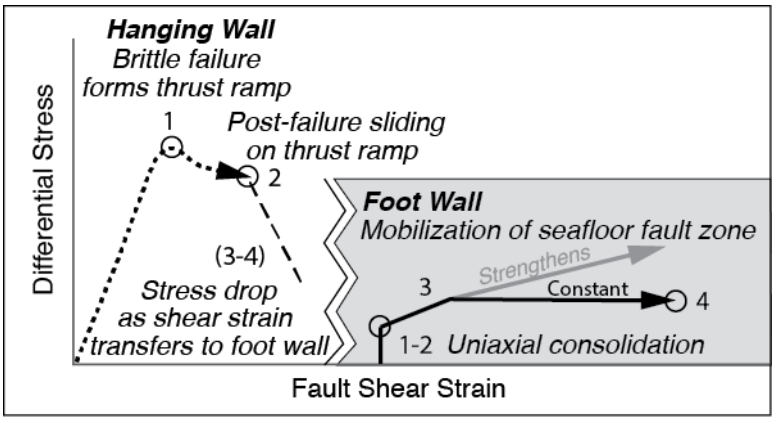
Hanging Wall
Brittle failure
forms thrust ramp
1
Post-failure sliding
on thrust ramp
2
Foot Wall
Mobilization of seafloor fault zone
(3-4)
Strengthens
3
Constant
4
Stress drop
as shear strain
transfers to foot wall
1-2 Uniaxial consolidation
Differential Stress
Fault Shear Strain

Figure 7